Supporting Information

Mann et al. 10.1073/pnas.0915022107

SI Materials and Methods

Cell Cultures. RAW264.7 and HEK-293T cells (American Type Culture Collection) were maintained in Dullbecco's modified Eagle's medium (DMEM) with 10% FBS, 2 mM L-glutamine, 100 U/mL penicillin, and 100 U/mL streptomycin at 37 °C with a 5% CO_2 atmosphere in a humidified incubator. RAW264.7 grown in α-MEM (Sigma) were induced to differentiate into osteoclast-like cells in the presence of 20 ng/mL M-CSF and 20 ng/mL RANKL (R&D Systems) for 72 h. Sealing zone-like structures were stained with FITC or TRITC-conjugated phalloidin (Sigma) or detected in cells stably expressing actin-GFP (20). TRAP-positive multinucleated osteoclasts (>3 nuclei) were identified by using a leukocyte acid phosphatase kit (Sigma), according to the manufacturer's instructions. For the bone resorption assay, RAW264.7 cells were induced to differentiate on thin slices of bovine tibia for 6 d. Bone slices were then washed and stained with Coomassie Brilliant Blue for identification of pit formation, as described (21). Stimulation of RAW264.7 cells toward macrophage activation was performed with 100 ng/mL LPS (Sigma) for 24 h. NO levels were determined by using Griess reagent (Sigma), according to the manufacturer's instructions. For Il-1α quantification, cells were stimulated with LPS for 10 h then fixed and stained with anti IL-1α antibody (R&D Systems). Viability and proliferation were measured with AlamareBlue metabolic assay (Biosource), according to the manufacturer's instructions.

miR-155 misexpression and knockdown miR-155 were transiently transfected with a miRVec pMSCV vector (22), or were retrovirally infected, to generate a miR-155 misexpressing RAW264.7 cell line. The 2'-O-methyl oligoribonucleotides against miR-155 (catalog No. AM13058; ABI), siGLO, and RISC-Free siRNA controls (Dharmacon) were transfected with Lipofectamine 2000 Reagent (Invitrogen), according to the manufacturer's instructions.

Microscopy, Image Acquisition, and Analysis. Microscopy-based data were acquired with a DeltaVision system (Applied Precision), consisting of an inverted IX70 microscope (Olympus), using Resolve3D software, and using the Priism software package (http://www.msg.ucsf.edu/IVE/index.html). Time-lapse and IL-1α$^+$ macrophages images were acquired by using the WiScan autofocus screening microscope (Idea Bio-Medical) (23). Quantification of absolute osteoclast number per well, the relative area occupied by giant multinucleated osteoclast per well, and the relative area stained with Coomassie Brilliant Blue on 0.5-cm^2 sections of bovine bone were marked manually and measured by using NIS-element software (Nikon).

Affymetrix Array Analysis and Bioinformatics. Total RNA was collected from RAW 264.7 cells, stably infected clones expressing miR-155, or an empty vector, by using the RNeasy Minikit (QIAGEN), according to the manufacturer's instructions. An Affymetrix Mouse Genome ST 1.0 microarray analysis was then performed by using pooled RNA from each group, according to manufacturer's protocols. Data were analyzed by using Rosetta Resolver Software. Microarray data were deposited in the GEO database under accession number GSE16749.

Quantitative PCR for mRNA and miRNA. Extraction of total RNA was carried out by using the miRNeasy Mini Kit (QIAGEN). Synthesis of cDNA and PCR was carried out by using the miScript PCR System (QIAGEN). The primer sequence is shown in Table S2. miRNA levels were normalized to the expression of the small RNA U6. mRNA expression was normalized to GAPDH and HPRT mRNAs

Western Blotting. Protein was isolated from RAW264.7 cells and used for Western blotting. The following antibodies were used for Western blotting: rabbit anti-PU.1 (T-21; Santa Cruz Biotechnology); mouse anti-MITF (a kind gift of David E. Fisher, Harvard Medical School, Boston) goat anti-GFP (Abcam), and mouse anti-Tubulin (SIGMA).

Assay of Luciferase Activity. The mouse MITF 3′ UTR target site (chr6:97969310–97970417) was subcloned into psiCHECK-2 Vector (Promega) and transfected into HEK293T cells, together with either miR-155 or miR-133 expressing vectors. Cells were harvested and assayed for Firefly and Renilla luciferase activity 48 h after transfection, according to manfacturer's instructions (Promega).

Statistical Analysis. All statistical analyses were performed by using a Microsoft Excel statistical software module. Results are given as mean ± SD. Statistical analyses were performed by means of the Student's *t* test; the null hypothesis was rejected at the 0.05 level.

1. Martin-Millan M, et al. (2010) The estrogen receptor-alpha in osteoclasts mediates the protective effects of estrogens on cancellous but not cortical bone. *Mol Endocrinol* 24:323–334.
2. Dai XM, Zong XH, Akhter MP, Stanley ER (2004) Osteoclast deficiency results in disorganized matrix, reduced mineralization, and abnormal osteoblast behavior in developing bone. *J Bone Miner Res* 19:1441–1451.
3. Katagiri M, et al. (2001) Mechanism of stimulation of osteoclastic bone resorption through Gas6/Tyro 3, a receptor tyrosine kinase signaling, in mouse osteoclasts. *J Biol Chem* 276:7376–7382.
4. Jurdic P, Saltel F, Chabadel A, Destaing O (2006) Podosome and sealing zone: Specificity of the osteoclast model. *Eur J Cell Biol* 85:195–202.
5. Kim K, Lee SH, Ha Kim J, Choi Y, Kim N (2008) NFATc1 induces osteoclast fusion via up-regulation of Atp6v0d2 and the dendritic cell-specific transmembrane protein (DC-STAMP). *Mol Endocrinol* 22:176–185.
6. Ory S, Brazier H, Pawlak G, Blangy A (2008) Rho GTPases in osteoclasts: Orchestrators of podosome arrangement. *Eur J Cell Biol* 87:469–477.
7. Bassett JH, Williams GR (2009) The skeletal phenotypes of TRalpha and TRbeta mutant mice. *J Mol Endocrinol* 42:269–282.
8. Ross FP, et al. (1993) Interactions between the bone matrix proteins osteopontin and bone sialoprotein and the osteoclast integrin alpha v beta 3 potentiate bone resorption. *J Biol Chem* 268:9901–9907.
9. Bai S, et al. (2005) FHL2 inhibits the activated osteoclast in a TRAF6-dependent manner. *J Clin Invest* 115:2742–2751.
10. Teitelbaum SL, Ross FP (2003) Genetic regulation of osteoclast development and function. *Nat Rev Genet* 4:638–649.
11. Kim K, et al. (2007) MafB negatively regulates RANKL-mediated osteoclast differentiation. *Blood* 109:3253–3259.
12. Zhao H, Laitala-Leinonen T, Parikka V, Väänänen HK (2001) Downregulation of small GTPase Rab7 impairs osteoclast polarization and bone resorption. *J Biol Chem* 276: 39295–39302.
13. Boyle WJ, Simonet WS, Lacey DL (2003) Osteoclast differentiation and activation. *Nature* 423:337–342.
14. Funaba M, et al. (1997) Increased cartilage and bone formation in spontaneously hypercholesterolemic rats. *Life Sci* 61:645–652.
15. Michou L, et al. (2010) Gene expression profile in osteoclasts from patients with Paget's disease of bone. *Bone* 46:598–603.
16. Hu R, et al. (2007) Eos, MITF, and PU.1 recruit corepressors to osteoclast-specific genes in committed myeloid progenitors. *Mol Cell Biol* 27:4018–4027.
17. Sugatani T, Hruska KA (2009) Impaired micro-RNA pathways diminish osteoclast differentiation and function. *J Biol Chem* 284:4667–4678.
18. Liu W, Wang S, Wei S, Sun L, Feng X (2005) Receptor activator of NF-kappaB (RANK) cytoplasmic motif, 369PFQEP373, plays a predominant role in osteoclast survival in part by activating Akt/PKB and its downstream effector AFX/FOXO4. *J Biol Chem* 280: 43064–43072.
19. Sato K, et al. (2006) Regulation of osteoclast differentiation and function by the CaMK-CREB pathway. *Nat Med* 12:1410–1416.

20. Luxenburg C, Parsons JT, Addadi L, Geiger B (2006) Involvement of the Src-cortactin pathway in podosome formation and turnover during polarization of cultured osteoclasts. *J Cell Sci* 119:4878–4888.
21. de Vries TJ, Schoenmaker T, Beertsen W, van der Neut R, Everts V (2005) Effect of CD44 deficiency on in vitro and in vivo osteoclast formation. *J Cell Biochem* 94:954–966.
22. Voorhoeve PM, et al. (2006) A genetic screen implicates miRNA-372 and miRNA-373 as oncogenes in testicular germ cell tumors. *Cell* 124:1169–1181.
23. Paran Y, et al. (2006) Development and application of automatic high-resolution light microscopy for cell-based screens. *Methods Enzymol* 414:228–247.

A

miRNA	Predicted Target	Effect
22	ESR1 (1), CSF1R (2), TYRO3 (3), WASF1 (4)	++
124	NFATC1 (5)	-
138	RHOC (6), THRB (7)	-
142-3p	WASL (4), ITGAV (8)	-
146a	TRAF6 (9)	-
148a	MITF(10), PTEN (10), ESR1(1)	-
152	WASL (4),MAFB (11)	-
155	PU.1 (10), CSF1R(10), MITF (10)	+++
186	RAB7 (12), MAPK1 (13), SP4 (13)	-
200c	SHC1 (14), MAP2K5 (15), PTPN12 (15)	-
221	ETS1 (16), MAPK6 (13), IKZF4 (16)	-
222	ETS1 (16), MAPK6 (13), IKZF4 (16)	-
223	NFI-A (17)	+
331	PKB (18)	-
422b	CREB (19), MAPK1 (10)	-

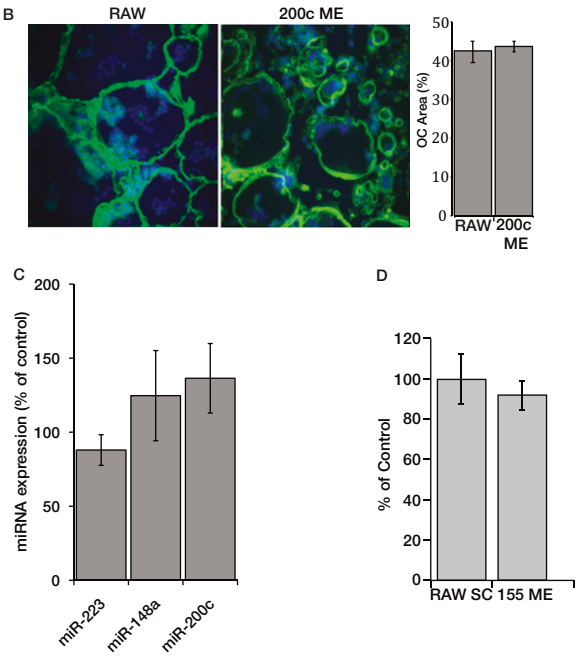

Fig. S1. A functional screen suggests miR-155 as a potential inhibitor of osteoclast differentiation. (*A*) A table showing a list of 15 miRNA genes and their predicted mRNA target that were misexpressed in RAW264.7 cells (refs. 1–19; see reference list above). The cultures were then induced with RANKL/M-CSF, and the relative effect of each of these miRNAs on osteoclast differentiation was evaluated in at least eight independent transfections. A minus sign means that the miRNA did not repress osteoclast differentiation. The number of plus signs (+, ++, +++) shows the estimated magnitude of inhibition endowed by the misexpression of a particular miRNA gene. (*B*) Representative micrograph from the screen described in *A*, exemplifying the inability of miR-200c to inhibit osteoclast differentiation. Quantification of the number of multinucleated osteoclasts per well was performed as described in *Results* (Fig. 1*A*) and is shown on the right (*C*) Expression levels of miR-223, miR-148, and miR-200c remained unchanged by miR-155 misexpression in RAW264.7 cells. (*D*) RAW264.7 cell viability and proliferation, evaluated by a metabolic assay (AlamareBlue) 4 d after misexpression of miR-155 (155 ME), is comparable with scrambled, nontargeting control oligos (RAW SC). Data from at least six independent experiments, performed in triplicates, are shown as mean ± SD. $*P < 0.01$.

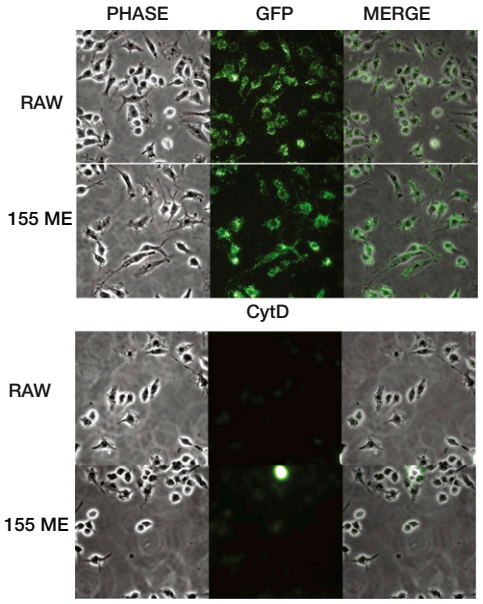

Fig. S2. miR-155 misexpression does not affect macrophage activation. Wild-type and miR-155 misexpressing cells were assayed for phagocytic activity by their ability to engulf fluorescent latex beads 6 h after LPS stimulation. Cytochalasin D, a membrane-permeable, potent inhibitor of actin polymerization, abrogates phagocytosis altogether and provides a negative control.

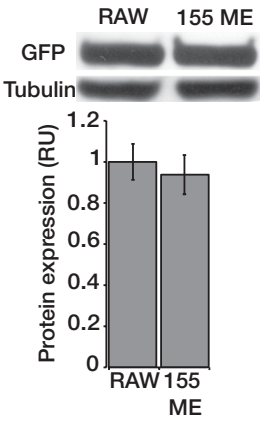

Fig. S3. Actin-GFP expression is not affected by mir-155 misexpression. Actin-GFP protein levels in cells stably expressing actin-GFP alone (RAW) or together with miR-155 (155 ME). Densitometry quantification of two independent Western blots, shown in relative units (RU).

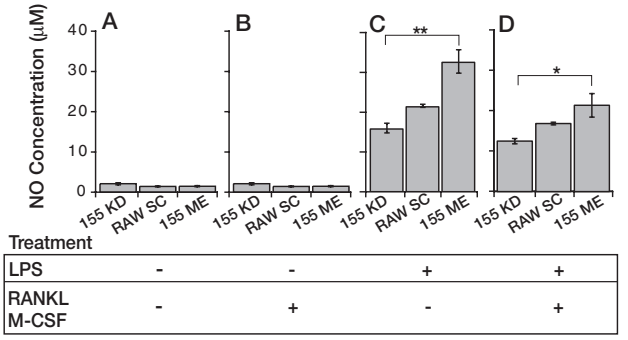

Fig. S4. miR-155 levels affect monocyte differentiation capacity when stimulated by conflicting proosteoclastic and inflammatory signals. Macrophage activity was assessed by nitric oxide (NO) production in cells transfected with scrambled, nontargeting oligonecleotides (RAW SC), cells misexpressing miR-155 (155 ME), or cells in which miR-155 was knocked down by antisense oligonucleotides (155 KD). Untreated cells (*A*); cells stimulated with RANKL and M-CSF (*B*); with LPS alone (*C*); and simultaneously, with a mixture of RANKL, M-CSF, and LPS (*D*). Data from at least three independent experiments, replicated eight times, are shown as mean ± SD. $*P < 0.05$; $**P < 0.01$.

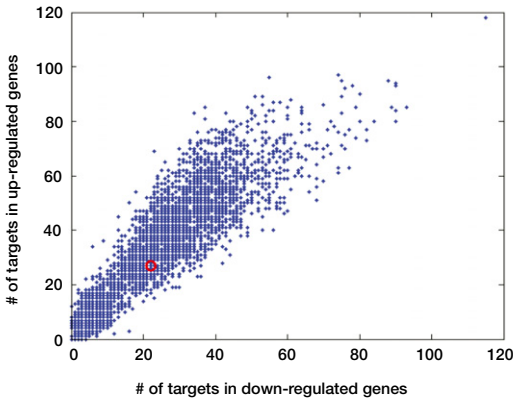

Fig. S5. Genes that are up-regulated upon RANKL/M-CSF treatment are not preferentially mir-155 predicted targets. Comparison of the number of predicted targets in a set of 234 up-regulated genes (*y* axis) vs. 366 down-regulated genes (*x* axis) for all (4,096) potential 6-mer words reveals that the mir-155 binding sequences, ("seed"), depicted at the center of the scatter plot by a red circle, do not exemplify any enrichment in the group of up-regulated genes.

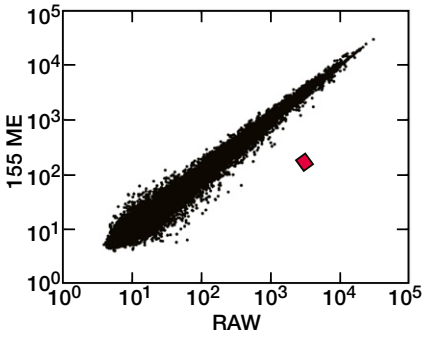

Fig. S6. GPNMB mRNA levels decrease significantly in progenitor cells misexpressing miR-155. A $\log_2$-scale scatter plot, presenting unmanipulated cells along the *x* axis (RAW) and miR-155 expressing cells (155 ME) along the *y* axis. GPNMB expression is marked by a red diamond.

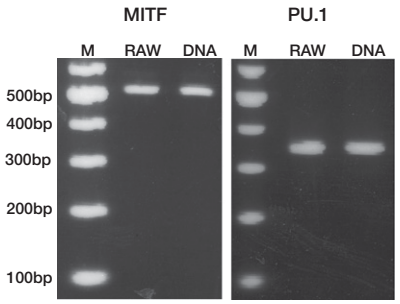

Fig. S7. The specific isoform of MITF and PU.1 3′UTRs expressed in RAW264.7 cells contains miR-155 binding sites. PCR for both MITF and PU.1 3′UTR fragments, flanking the miR-155 binding sites, was conducted both for RAW264.7 cDNA (RAW) and genomic DNA (DNA). A single band in the expected size suggests that the isoform expressed may be subject to miR-155 regulation.

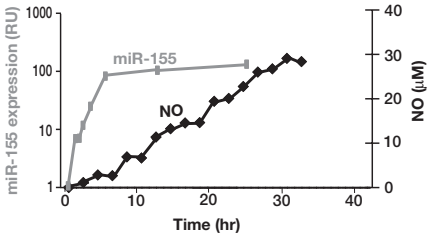

Fig. S8. A detailed temporal analysis of miR-155 expression (gray, $\log_{10}$ scale; *y* axis on the left) and nitric oxide (NO) synthesis (black, linear scale; *y* axis on the right) in RAW264.7 cells stimulated with LPS.

Table S1. Gene expression profiles of 500 mRNA in RAW264.7 control cells and cells misexpressing miR-155 during osteoclast differentiation. Raw data presented in Fig. 4*A*: Log_2 expression levels of the 500 mRNAs whose expression are most significantly differentiated, sorted according to the relative difference between RAW264.7 cells, and RAW264.7 cells in which miR-155 is misexpressed

Table S1 (DOC)

Table S2. Primers used for QRT-PCR analysis

Table S2 (DOC)

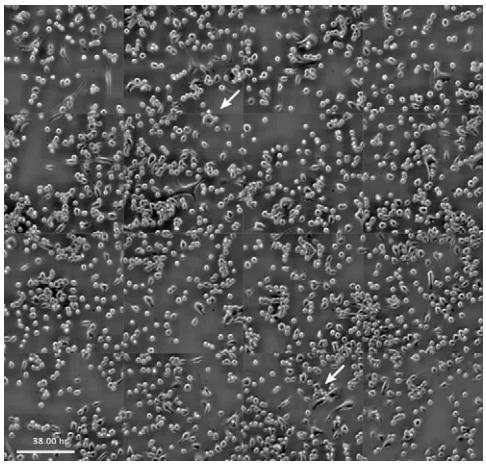

Movie S1. Cell fusion during osteoclast differentiation. Time-lapse imaging of RAW264.7 control cells after RANKL and M-CSF stimulation. Imaging begins 40 h after addition of cytokines (15 min per frame) and continues for 30 h. Arrows indicate early fusion events. (Scale bar: 100 μm.)

Movie S1

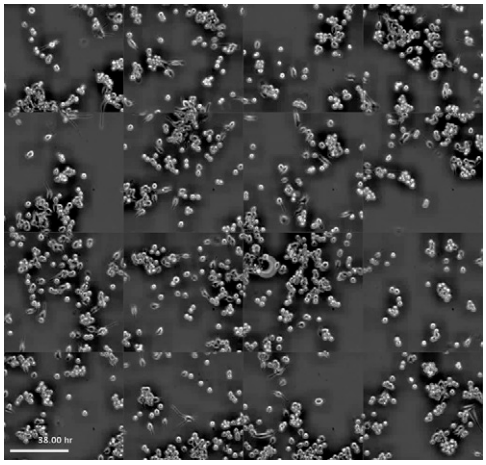

Movie S2. miR-155 misexpression impairs fusion. Time-lapse imaging of RAW264.7 cells misexpressing miR-155 after RANKL and M-CSF stimulation. Imaging begins 40 h after addition of cytokines (15 min per frame) and continues for 30 h. (Scale bar: 100 μm.)

Movie S2